

The effect of dispersoids on the micromechanisms of crack extension in Al-Mg-Si alloys

J. A. BLIND*, J. W. MARTIN

Department of Metallurgy and Science of Materials, University of Oxford, Parks Road, Oxford, UK

The effect of an increasingly triaxial stress state on the fracture strain of peak-aged alloys was measured using a series of notched tensile specimens. The alloy ductility was found to increase with dispersoid content and to decrease with increased stress triaxiality. Crack tip plastic zone sizes on the midplane of compact tension specimens were measured experimentally and, for the same applied stress intensity factor, were found to decrease with increasing dispersoid content. SEM analysis of the fracture surfaces revealed that the dominant micromechanism of crack extension was ductile rupture along the grain boundary precipitate free zone. These results are discussed in terms of the influence of dispersoids on slip distribution. The stress and strain distributions in the plastic zones are related to the micromechanisms of crack extension.

1. Introduction

In the peak-aged condition, Al-Mg-Si alloys are susceptible to a low ductility intergranular fracture [1]. The presence of a 0.1 μm diameter incoherent dispersoid phase, by the addition of certain transition elements such as manganese, has been found to improve ductility [2] and toughness [3], although the failure mode remains primarily intergranular. Lohne and Naess [4] maintain that the effect of the dispersoids is primarily to produce a fine grain size, but Dowling and Martin [5] and Prince and Martin [6] attribute these dispersoid effects to the homogenization of slip distribution. They proposed a fracture model based on a postulated critical local strain that must be achieved at the head of a slip band to cause an increment of crack propagation; since dispersoids homogenize slip distribution, a larger macroscopic strain must be applied to achieve the critical local strains.

The present study was undertaken on a series of alloys of carefully controlled grain size in order to clarify the conditions of stress and strain ahead of a crack tip that are required to cause crack exten-

sion in these alloys, as the dispersoid content is varied.

2. Experimental techniques and results

2.1. Materials

Alloy composition, grain sizes and mechanical properties are shown in Table I. The compositions were chosen to systematically increase the volume fraction of manganese-bearing dispersoids of the $\alpha(\text{Al}_{12}\text{Mn}_3\text{Si})$ phase. It should be noted that, with the exception of the ternary alloy MT, the alloys had similar grain sizes and yield strengths and were in the peak-aged condition. The iron content of the alloys was kept quite low in order to minimize the inclusion particles which might mask the influence of the dispersoids. However, one alloy, designated MC, contained the commercial level of iron impurity content to enable a comparison with the inclusion free alloys.

Standard tensile test parameters also shown in Table I include the 0.2% offset yield strength σ_y , the ultimate strength σ_u , the work hardening exponent N and the true strain to fracture ϵ_f . These

* Present address: Department of Engineering Mechanics, US Air Force Academy, Colorado, 80840, USA.

TABLE I Alloy compositions and mechanical properties

Designation	Compositions (wt %)				Grain size (μm)	Volume fraction dispersoids (%)	$\sigma_y(0.2\%)$ (MPa)	σ_u (MPa)	N from $\sigma = kE^N$	ϵ_f
	Mg	Si	Fe	Mn						
MT	0.63	1.07	<0.01	<0.01	200	—	280	315	0.050	0.08
ML	0.59	0.99	<0.01	0.21	100	0.22	320	350	0.051	0.24
MM	0.61	1.02	0.06	0.44	85	0.45	310	350	0.054	0.29
MH	0.61	1.02	0.01	0.61	80	0.61	320	380	0.062	0.26
MC	0.60	1.02	0.30	0.58	75	0.80	310	355	0.062	0.40

values represent averages for at least three tests on Hounsfield type tensile specimens having a diameter of 8 mm and a gauge length of 10 mm. Tests were performed on a closed loop servo-hydraulic testing machine operating in displacement control at a strain rate of 0.01 min^{-1} . A modified strain gauge extensometer was used to continuously measure specimen diameter.

2.2. Notched tensile tests

The response of the materials to varying degrees of triaxial stress state was measured on circumferentially notched tensile specimens. The specimen geometry was based on the work of Mackenzie *et al.* [7]. The effective plastic strain to failure initiation was measured for different values of stress triaxially by varying the notch root radius of curvature.

The specimen geometry and notch radii are shown in Fig. 1. Ductile failure in this geometry has been found to initiate at the centreline of the specimen in the notch where the stress state is most severe [7]. Using the stress and strain analy-

sis of this geometry due to Bridgman [8], the stress triaxiality on the centreline can be defined as the ratio of the mean stress, σ_m , to the effective stress, $\bar{\sigma}$, as:

$$\frac{\sigma_m}{\bar{\sigma}} = \frac{1}{3} + \ln\left(\frac{c}{2R} + 1\right) \quad (1)$$

where

$$\sigma_m = \frac{\sigma_1 + \sigma_2 + \sigma_3}{3} \quad (2)$$

$$\bar{\sigma} = \frac{2^{1/2}}{2} [(\sigma_1 - \sigma_2)^2 + (\sigma_2 - \sigma_3)^2 + (\sigma_3 - \sigma_1)^2]^{1/2} \quad (3)$$

In these equations, σ_1 , σ_2 , and σ_3 are the principal stress, c is the specimen radius and R is the notch root radius of curvature.

The effective plastic strain $\bar{\epsilon}_p$ is given by

$$\bar{\epsilon}_p = 2 \ln\left(\frac{c_0}{c}\right) \quad (4)$$

where c_0 denotes the original specimen radius. Hancock and Mackenzie [9] determined that

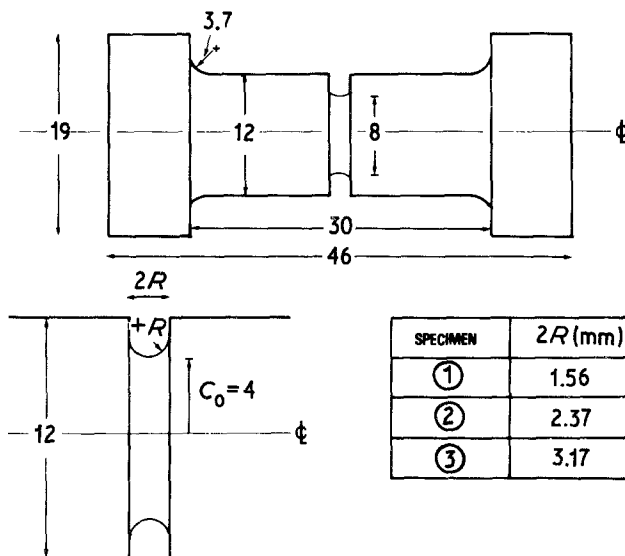


Figure 1 Notched tensile specimen. Dimensions are in mm. Values of notch root diameter ($2R$) are also shown.

failure initiation in a particular specimen corresponds to the maximum in the plot of true stress against effective plastic strain. In some materials, there may be a considerable amount of strain between this point of failure initiation and subsequent final fracture of the specimen. However, this was not the case in the present study and the failure strain was taken as the effective plastic strain at fracture $\bar{\epsilon}_f$. Results are presented in Fig. 2 for each alloy in the form of $\bar{\epsilon}_f$ against stress triaxiality $\sigma_m/\bar{\sigma}$. These results show that alloy MT has a very low fracture strain at all stress triaxialities tested. The fracture strains of alloys ML and MM, though progressively higher, are not strong functions of $\sigma_m/\bar{\sigma}$. Alloys MH and MC both show a more pronounced decrease in $\bar{\epsilon}_f$ at high stress triaxialities with alloy MC actually becoming slightly less ductile than alloy MH.

2.3. Toughness

The ductile fracture toughness J_{IC} for each alloy was determined using the multiple specimen compact tension test piece technique outlined by the ASTM Committee E-24 on Fracture Testing [10].

Details of the experimental method are given elsewhere [11]. However, the resulting J_{IC} values are presented in Table II. Thus, the ductile fracture toughness at incipient crack extension is seen to increase with dispersoid content for alloys having similar grain sizes and yield strengths.

For later analysis, it was desirable to know the values of applied stress intensity factor K_0 and crack tip opening displacement δ_0 at the onset of crack extension. Since there was no direct method available capable of detecting the onset of crack extension under elastic-plastic conditions of slow stable crack growth, an indirect method was developed using the area under the experimental load-load line displacement traces for the J test compact tension specimens. Once J_{IC} had been determined for a particular alloy, the area A_0 under each particular load (P)–load line displacement (δ_{LL}) trace corresponding to incipient crack extension was calculated from

$$A_0 = \left(\frac{1 + \alpha^2}{1 + \alpha} \right) \frac{J_{IC} B b}{2} \quad (5)$$

where α is a geometric factor defined in [10],

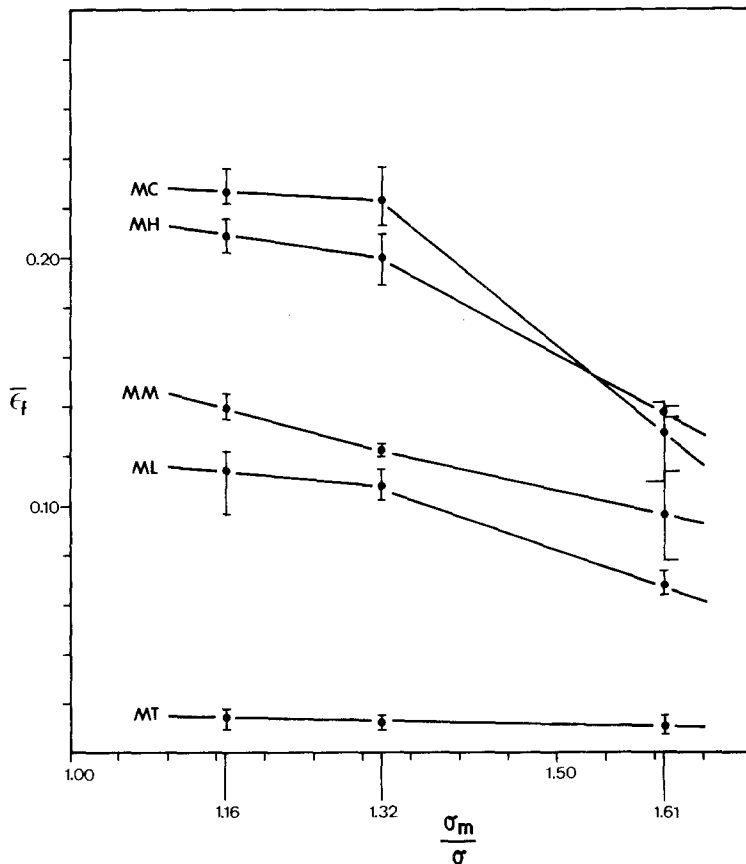


Figure 2 Effective plastic strain at failure versus stress triaxiality for notched tensile specimens. Error bars show full range of values.

TABLE II Experimentally determined parameters for each alloy

Alloy	J_{IC} ($N\text{ mm}^{-1}$)	K_0 ($MPa\text{ m}^{1/2}$)	δ_0 (μm)	α	r_{p0} (μm)
MT	11.2	27.4 ± 1.8	60 ± 10	0.012	115
ML	19.5	36.8 ± 0.9	68 ± 10	0.034	460
MM	25.2	41.2 ± 0.9	75 ± 5	0.025	440
MH	30.2	43.5 ± 1.0	93 ± 5	0.023	420
MC	26.6	44.8 ± 1.71	81 ± 7	0.017	350

B is specimen thickness and b is the remaining ligament length. The point on the $P-\delta_{LL}$ trace that gave this area was taken as the point of crack extension onset and values for P_0 and δ_{LL0} thus determined. K_0 was calculated from P_0 using the equation from the ASTM standard E399-78 [12]. The value of δ_0 was calculated from δ_{LL0} assuming the hinge model of a compact tension specimen [13] with a hinge rotation factor of 0.195. The average values for K_0 and δ_0 are also shown in Table II, error figures representing the standard deviation of at least four tests.

2.4. Crack tip plastic zone size

The size of the crack tip plastic zone, r_p , is theoretically predicted to be proportional to the square of the applied stress intensity factor, K , as

$$r_p = \alpha \left(\frac{K}{\sigma_y} \right)^2 \quad (6)$$

where α is a constant of proportionality depending on the state of stress and the direction of measurement from the crack tip. To evaluate for the alloys in the present study, crack tip plastic zones on the mid-plane of 11.5 mm thick CT specimens were mapped using the electron channelling pattern (ECP) technique to detect the location of the elastic-plastic interface. Details of the technique may be found in [6]. Using tensile specimens pulled to known values of plastic strain, it was found that the ECP technique of the present study was capable of detecting plastic strains of less than 1%. An example of the resulting experimentally determined crack tip plastic zone is shown in Fig. 3. As indicated, the distance measured directly ahead of the crack tip to the elastic-plastic boundary was taken as r_p . After mapping the plastic zone for each alloy for different applied K values, the variation in α from Equation 6 with dispersoid content was established. Results are shown in Fig. 4 and values of α are listed in Table II. The lines of Fig. 4 represent the best fit for each alloy and are extrapolated out to the value of the abscissa

corresponding to the onset of crack extension i.e. $(K_0/\sigma_y)^2$ for each alloy. Thus, the values of the crack tip plastic zone size at the onset of crack extension, r_{p0} , were also obtained and are listed in Table II.

2.5. Fractography

Fracture surfaces of compact tension specimens were examined and Fig. 5 shows a low magnification view of a mechanically polished crack tip region of alloy ML. The surface shown is from the specimen mid-plane and perpendicular to the plane of the crack (crack propagation direction

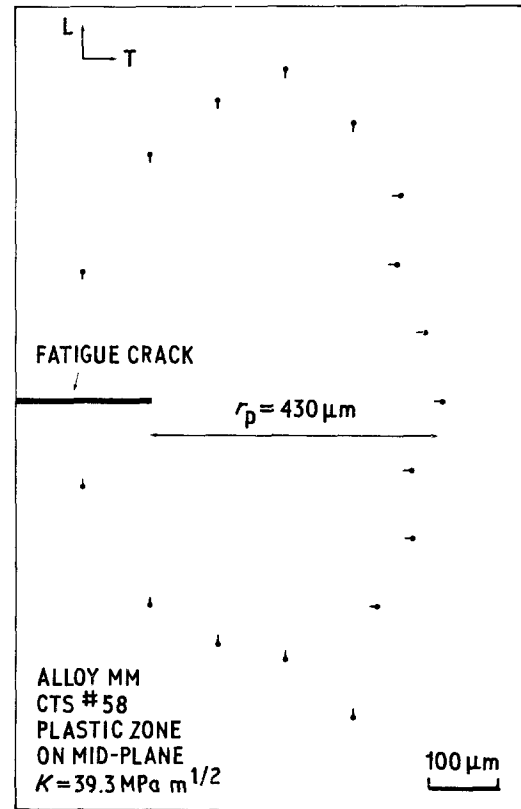


Figure 3 An example of a mid-plane crack tip plastic zone as obtained using the electron channelling pattern (ECP) technique.

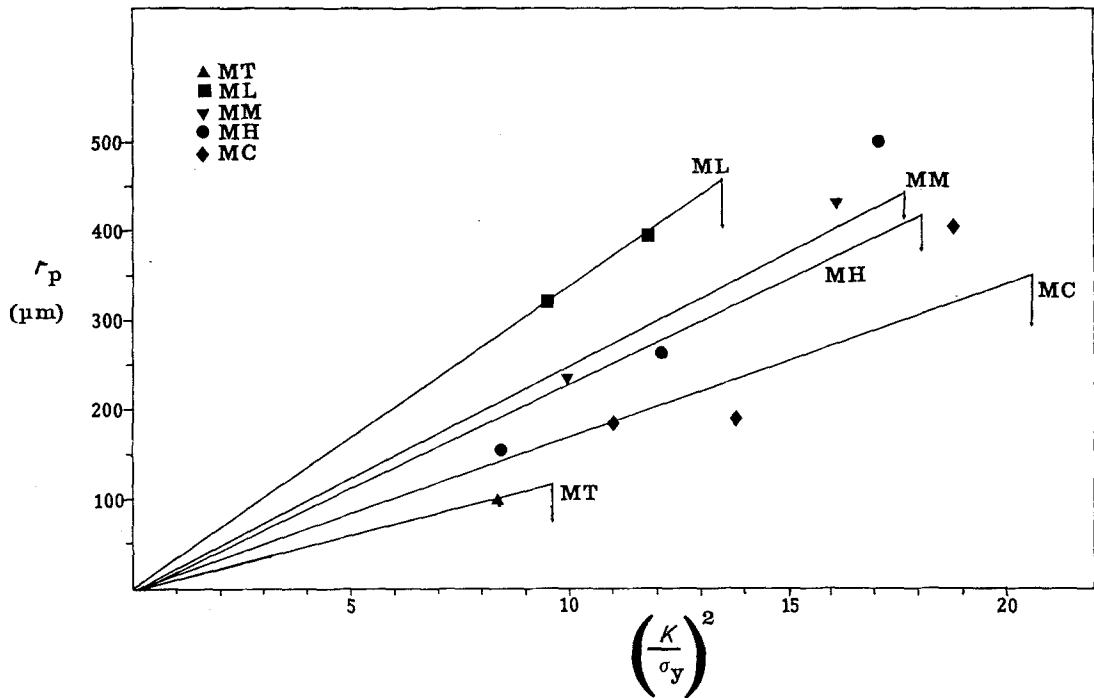


Figure 4 Crack tip plastic zone sizes, r_p , as a function of applied stress intensity factor, K , and yield stress, σ_y . Arrows point to the values of $(K/\sigma_y)^2$ that correspond to the onset of crack extension.

is from top to bottom). This specimen was loaded to a K of $34.5 \text{ MPa m}^{1/2}$ which is less than K_0 ; however, microcracks in the form of separated grain boundaries are evident in front of the macroscopic crack tip. Higher magnification of these grain boundary microcracks revealed tiny ($< 1 \mu\text{m}$) dimples on the grain boundary fracture surfaces. The occurrence of these microcracks prior to general crack extension will be considered again later.

Fractographs showing progressively higher magnification of the monotonic fracture surface in alloy MT are shown in Fig. 6. In Fig. 6a, the grain facets clearly indicate an intergranular fracture mode. However, in Fig. 6b it can be seen that the intergranular facets are covered with fine scale dimples, and in Fig. 6c the dimples contain particles of the order of 0.05 to $0.1 \mu\text{m}$ diameter. The dimples appear to be shallow and connected by thin walls that have formed at the moment of coalescence and final separation of the fractured faces. Since there is a particle located roughly centrally in almost every dimple, it is suggested that the intergranular fracture mode occurs by a process of grain boundary ductile rupture. This grain boundary ductile rupture occurs by void nucleation at grain boundary particles and void

growth in the plane of the grain boundary along the precipitate free zone (PFZ). That this is a relatively low energy fracture mode can be inferred from Fig. 6b where a secondary crack is

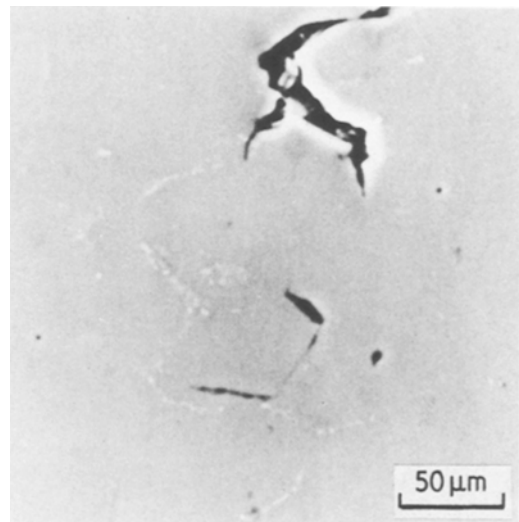


Figure 5 Low magnification view of mechanically polished crack tip region of alloy ML. $K = 34.5 \text{ MPa m}^{1/2}$. Crack propagation direction is from top to bottom. Grain boundaries have opened up in the region in front of the crack tip.

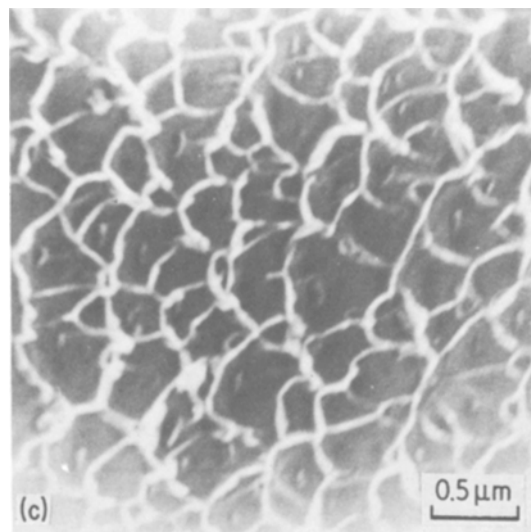
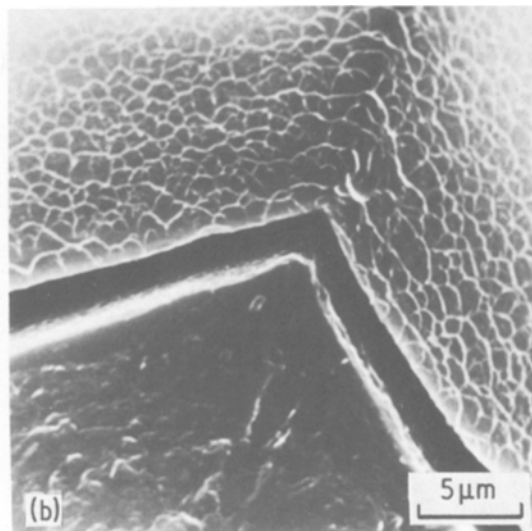
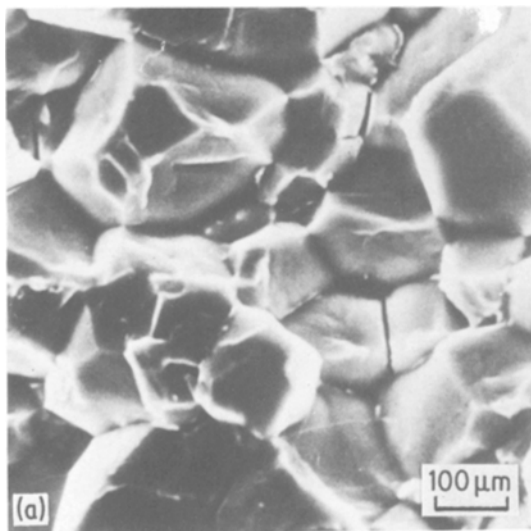


Figure 6 Fracture surface of alloy MT. (a) Low magnification of intergranular facets. (b) Fine dimples on intergranular surfaces. (c) Intergranular dimples containing particles.

ductility, the dispersoid containing alloys also fractured predominantly by the grain boundary ductile rupture mode. In Fig. 7 the intergranular facets of alloy ML can be seen to have a rough, dimpled appearance similar to alloy MT. A fractured inclusion from alloy MH is shown in Fig. 8, however there is only a limited amount of plasticity evident around the inclusion. The fine scale intergranular dimples can also be seen clearly.

Alloy MC, which had a high iron content and

seen to have intersected the primary fracture surface. This bifurcated crack front was common in the ternary alloy MT and reflects the fact that the highly plastically deformed material was confined to the PFZ. Prior to fracture, continuity requires that the total strain, i.e. elastic plus plastic, in the PFZ be the same as in the grain interior. Thus, the PFZ would have a slightly higher plastic strain due to its lower yield strength. However, once the grain boundary ductile rupture process initiates, the elastic strain in the grain interior can be relieved by the plastic separation process of void growth and coalescence in the PFZ, giving the dimples of Fig. 6c.

Although there was greater fracture surface distortion due to smaller grain size and higher

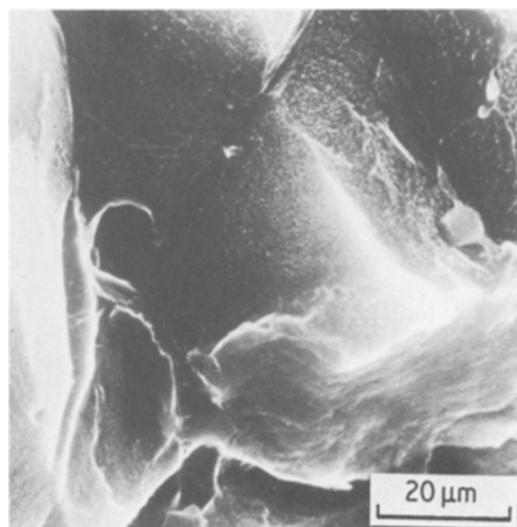


Figure 7 Fracture surface of alloy ML. Dimpled structure is evident on intergranular regions.

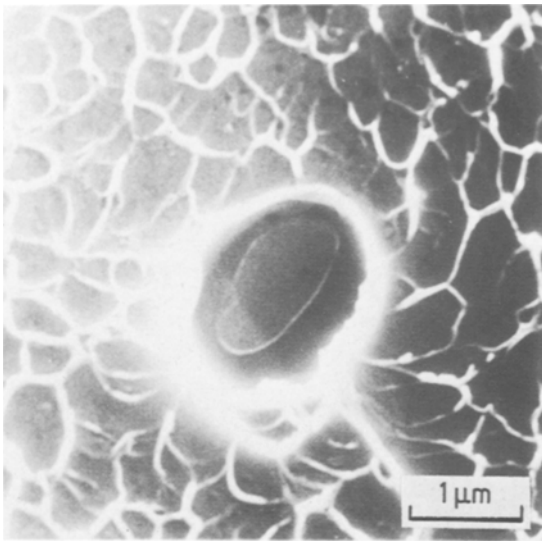


Figure 8 Fracture surface of alloy MH, the fractured inclusion is surrounded by fine intergranular dimples.

therefore a high amount of inclusions, fractured with approximately equal contributions of intergranular ductile rupture and transgranular ductile rupture due to the coarse particles.

3. Discussion

3.1. Stress and strain distributions

The pronounced increase in toughness with dispersoid content for the alloys in the present study suggests that dispersoids increase the necessary stresses and/or strains at the crack tip for the predominant fracture micromechanism to operate. The nature of the stress and strain distributions within the plastic zone can be inferred from the work of Rice and Johnson [14] which considered the effects of crack tip blunting. The resulting graphical solutions present the stress and strain distributions as functions of X/δ where X is the position of a point in front of the initially sharp crack and δ is the CTOD. Considering first the stress distribution, Rice and Johnson [14] in their Fig. 10 present approximate modified stress distributions (σ_{yy}/σ_y) which depend on the initial yield strain, σ_y/E , and work hardening exponent, N . These curves are shown in Fig. 9 (with σ_y/E taken as 0.005) for N equal to 0 and 0.10. Since N is approximately 0.05 for the present alloys, the middle curve was interpolated from the Rice and Johnson results. There, the present alloys are

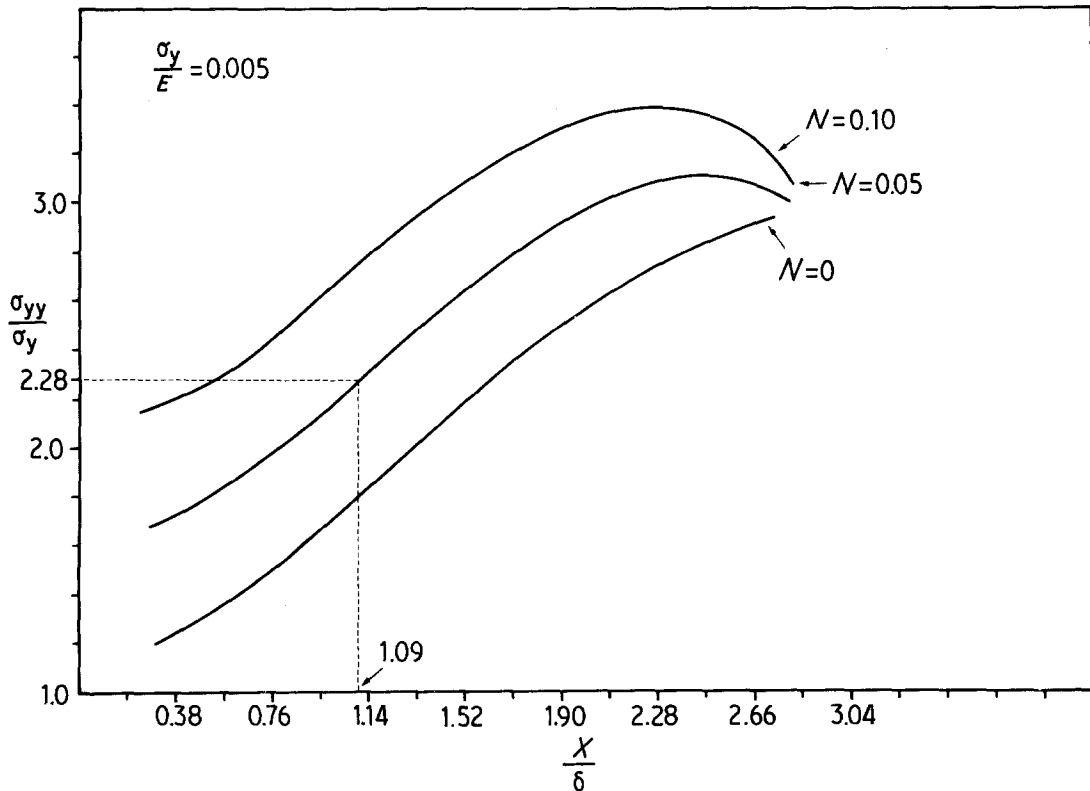


Figure 9 Modified stress distribution due to crack tip blunting, taken from Rice and Johnson [14] Fig. 10 for $\sigma_y/E = 0.005$. The most highly triaxial notched tensile specimen gives σ_{yy}/σ_y of 2.28 which corresponds to X/δ of 1.09.

TABLE III Boundary conditions and constants for Equation 7

Alloy	BC [1]	BC [2]	A	B
	δ_0/r_{p0} for $\bar{\epsilon}_p = 0$	$\bar{\epsilon}_f$ for $X/\delta = 1.09$		
MT	0.522	0.011	0.028	-0.0145
ML	0.152	0.068	0.089	-0.0135
MM	0.170	0.097	0.130	-0.0221
MH	0.233	0.138	0.202	-0.0470
MC	0.231	0.130	0.190	-0.0438

subjected to a maximum achievable stress that is just over three times the yield stress and occurs at about 2.5 crack opening displacements in front of the tip. Since the values of N are similar for the present alloys, the larger δ_0 (see Table II) with increased dispersoid content means that the maximum stress occurs further in front of the crack tip. However, the maximum absolute value of σ_{yy} would not change (since σ_y is essentially the same for each). This indicates that the predominant fracture mechanism is not simply stress controlled since, if it were, a larger δ_0 would not be required.

Rice and Johnson [14] also plot the effective plastic strain as a function of X/δ , shown in Fig. 10, for small scale yielding and fully plastic conditions. The small scale yielding curve predicts zero plastic strain at approximately two CTODs in front of the crack tip. This is clearly not applicable to the present alloys since the plastic zone size at crack extension onset, r_{p0} , was up to six times larger than δ_0 (see Table II). Also, the notched tensile test results showed that dispersoids increase the effective plastic strain at fracture for the same stress triaxiality. It therefore seems reasonable to

assume that the strain distribution in front of the crack tip changes from alloy to alloy and that the change is controlled by the dispersoid content. The following summarizes an attempt to describe the magnitude of the strain distribution change.

Taking the general form of the plastic strain distribution from Rice and Johnson [14], one obtains:

$$\bar{\epsilon}_p = A \left(\frac{\delta}{X} \right) + B \quad (7)$$

Solving for the constants A and B for each alloy requires two boundary conditions. The first sets $\bar{\epsilon}_p$ equal to zero at the elastic-plastic interface, i.e. at $(\delta/X) = (\delta_0/r_{p0})$. The second boundary condition invokes the fracture strain of the most highly triaxial notch tensile specimen geometry. The most severe notch corresponds to σ_{yy}/σ_y of 2.28, and from Fig. 9, this stress state occurs at X/δ equal to 1.09. Therefore, the second boundary condition is $\bar{\epsilon}_p = \bar{\epsilon}_f$ at $X/\delta = 1.09$. These boundary conditions and the resulting values of A and B are given in Table III. Due to the assumptions involved, these values of A and B should be taken only to provide a reasonable comparison of the strain distributions in front of a blunting crack tip as a function of dispersoid content.

Now, the strain profiles in the crack tip plastic zone at the onset of crack extension can be compared by substituting δ_0 , A and B into Equation 7. The resulting profiles are shown in Fig. 11. The plastic zone size at the onset of crack extension, r_{p0} , is shown for each alloy on the abscissa. When presented in this way, several points become clear. At the onset of crack extension, alloy MT sustains high strains over only a very short distance. Due

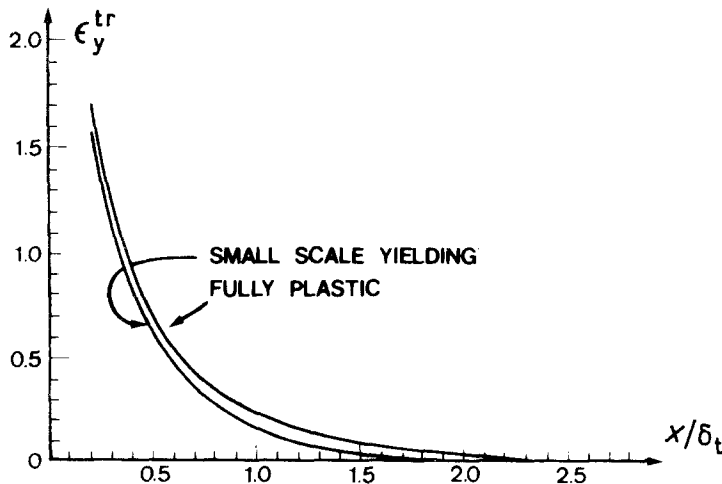


Figure 10 True strain on the line ahead of a blunting crack tip as a function of distance, X of a material point from the tip before deformation divided by the crack opening displacement, (from Rice and Johnson [14]).

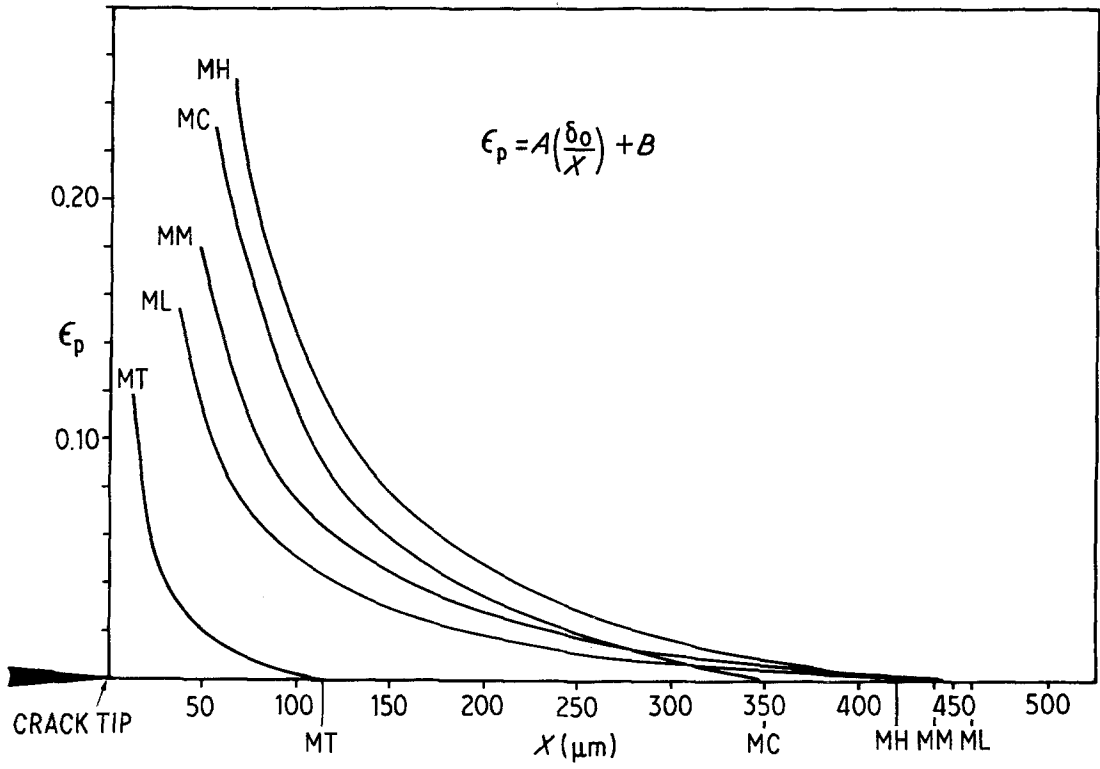


Figure 11 Effective plastic strain versus distance ahead of the crack tip from Equation 7, shown at the onset of crack extension.

to the intense slip bands that form, strain concentrations (and therefore stress concentrations) are created at the grain boundaries. Conditions for void nucleation at grain boundary particles are satisfied quickly and low energy ductile rupture occurs along the PFZ. For the dispersoid containing alloys, the plastic zone sizes at crack extension onset are similar, but the strain profiles reflect the increase in strain required for fracture as dispersoids homogenize the slip. As a fracture criterion, this is equivalent to saying that the critical strain

must be achieved over a larger critical distance. Thus, in this series of alloys, the critical microstructural distance increases with slip homogenization. The results for alloy MC indicate that this is true only so long as the fracture mechanism does not change. The lower strain profile at crack extension for alloy MC reflects the decrease in the critical distance caused by the presence of coarse inclusions. These coarse inclusions serve as void nucleation sites for the transgranular ductile rupture mechanism which is superimposed on the

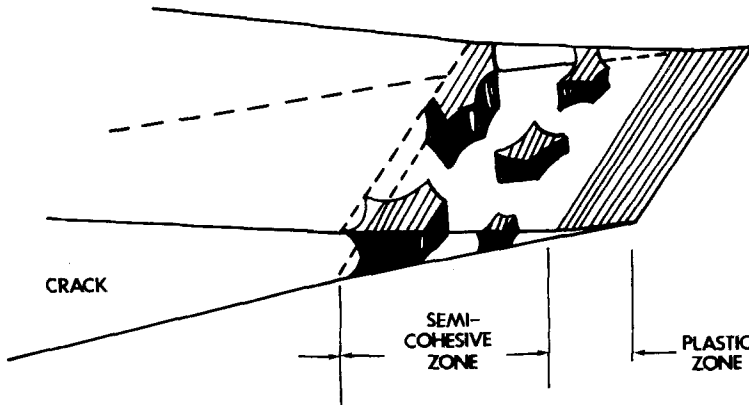


Figure 12 Schematic of crack tip, semi-cohesive zone and plastic zone. Shaded areas represent unfractured ligaments (from Gerberich and Moody [15]).

grain boundary ductile rupture mechanism, resulting in fracture at lower strains.

3.2. Fracture model

As was shown in Fig. 5, short microcracks were often observed in the plastic zone ahead of the main crack tip on specimens loaded to a stress intensity less than that required for the onset of crack extension. Also, from the previous discussion, the criterion for grain boundary ductile rupture will be satisfied in a region in front of the crack tip, under the appropriate combination of high principal tensile stress, high stress triaxiality and intense slip bands. A useful model to describe this concept is the semi-cohesive zone suggested by Gerberich and Moody [15] in which the crack tip region contains areas that have fractured separated by unfractured ligaments. Moody and Gerberich [16] used this model to predict successfully the grain size effect on the fatigue threshold stress intensity in titanium alloys, but the model is equally applicable to the monotonic loading crack extension mechanisms of the present study. A schematic of the semi-cohesive zone model is shown in Fig. 12. At the tip of the main crack lies a plastic zone that contains within it the semi-cohesive zone. As the load is increased, the plastic zone grows larger and certain grain boundaries that are favourably oriented to the maximum tensile stress will fracture by microvoid coalescence along the PFZ. When dispersoids are present, since they suppress this fracture micromechanism, fewer of these grain boundaries open up ahead of the crack tip and more unfractured ligaments remain in the semi-cohesive zone. Macroscopic crack extension then corresponds to the fracture of the remaining ligaments and the joining of the macrocracks to the main crack. As the volume fraction of dispersoids increases, slip becomes more homogeneous and the tendency for intergranular ductile rupture is reduced. Thus, a larger CTOD is required for crack extension onset and larger fracture toughnesses result. The semi-cohesive zone model also applies to the alloy MC. However, due to its much larger number of coarse constituent particles, the opening up ahead of the crack tip is due to both intergranular ductile rupture and coarse particle ductile rupture. Thus, even though alloy MC has more dispersoids and, therefore, more homogeneous slip than alloy MH, the fracture toughness is decreased due to the coarse constituent particles.

4. Summary and conclusions

1. The fracture strain of peak-aged Al–Mg–Si alloys increases with dispersoid content and decreases with increased stress triaxiality.

2. For the same applied stress intensity, the crack tip plastic zone sizes decrease with increasing dispersoid content.

3. Crack extension is by ductile rupture along the grain boundary PFZ, with microcracks forming in the plastic zone ahead of the main crack, thus forming a “semi-cohesive” zone.

4. Application of the Rice and Johnson [14] analysis enables a comparison to be made of the strain distributions ahead of a blunting crack tip as a function of dispersoid content.

5. The plastic zone sizes at crack extension are similar for the dispersoid-containing alloys, but the strain profiles reflect the increase in strain required for fracture as dispersoids homogenize the slip. Thus the critical microstructural distance increases with slip homogenization.

6. Dispersoids inhibit microcrack formation in the semi-cohesive zone, and therefore, increase the resistance to crack extension.

Acknowledgements

The authors are indebted to Messrs Alcan International Limited for supplying the alloys, to Professor P. B. Hirsch, FRS, for provision of laboratory facilities, and to Dr L. Edwards and Mr J. S. Crompton for many helpful discussions. JAB acknowledges financial support from the US Air Force.

References

1. R. CHADWICK, N. B. MUIR and N. B. GRAINGER, *J. Inst. Met.* **82** (1953) 75.
2. J. M. DOWLING and J. W. MARTIN, *ICF4*, Waterloo, Canada **2** (1977) 87.
3. B. J. DUNWOODY, J. M. MOORE and A. T. THOMAS, *J. Inst. Met.* **101** (1973) 172.
4. O. LOHNE and I. J. NAESS, *ICSMA5*, Aachen **2** (1979) 781.
5. J. M. DOWLING and J. W. MARTIN, *Acta Met.* **24** (1976) 1147.
6. K. C. PRINCE and J. W. MARTIN, *ibid.* **27** 1401.
7. A. C. MACKENZIE, J. W. HANCOCK and D. K. BROWN, *Eng. Fract. Mech.* **9** (1977) 167.
8. P. W. BRIDGMAN, “Studies in Large Flow and Fracture” (McGraw-Hill, New York, 1952).
9. J. W. HANCOCK and A. C. MACKENZIE, *J. Mech. Phys. Solids* **24** (1976) 147.
10. G. A. CLARKE and J. D. LANDES, *J. Test. Eval.* **7** (1979) 264.
11. J. A. BLIND and J. W. MARTIN, *Mater. Sci. Eng.*

- 57 (1983) 49.
12. ASTM E399-78, "Standard Method of Test for Plane-Strain Fracture Toughness of Metallic Materials" (ASTM, Philadelphia 1978).
 13. J. W. PONTON and G. M. C. LEE, *J. Strain Anal.* **15** (1980) 31.
 14. J. R. RICE and M. A. JOHNSON, "Inelastic Behaviour of Solids", edited by M. F. Kanninen *et al.* (McGraw-Hill, New York, 1970) pp. 641-72.
 15. W. W. GERBERICH and N. R. MOODY, *ASTM STP* **675** (1979) pp. 292-341.
 16. N. R. MOODY and W. W. GERBERICH, *Met. Sci.* **14** (1980) 95.

*Received 15 July
and accepted 20 September 1982*